ELSEVIER

Transient modelling of a multi-cell alkaline electrolyzer for gas crossover and safe system operation

Check for updates

Silvestros Oikonomidis [a], Mahinder Ramdin [a], Othonas A. Moultos [a], Albert Bos [b], Thijs J.H. Vlugt [a], Ahmadreza Rahbari [a,b,*]

[a] *Engineering Thermodynamics, Process & Energy Department, Faculty of Mechanical, Maritime and Materials Engineering, Delft University of Technology, Leeghwaterstraat 39, 2628CB, Delft, the Netherlands*
[b] *Headquarters, XINTC B.V., Loubergweg 22-24, 6961 EK, Eerbeek, the Netherlands*

HIGHLIGHTS

- A transient model is developed to predict gas crossover in an alkaline electrolyzer.
- Model can be used for multi-cell stacks with two separator tanks.
- Dynamic response of the system depends strongly on the size of the separator tanks.
- The model computes different product gas impurities depending on the start-up mode.
- This is a tool to size the stack and separator tanks, considering explosion safety.

GRAPHICAL ABSTRACT
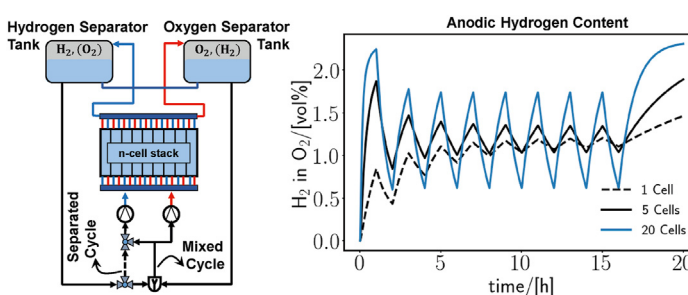
ABSTRACT

Due to the intermittency of renewable energy sources, alkaline water electrolyzers are typically operated at partial load compared to the nominal design value. It is well-known that gas crossover is dominant at low current densities leading to higher anodic hydrogen content and higher cathodic oxygen content in the separator tanks. High anodic hydrogen content is tantamount to loss of product hydrogen which results in an explosive atmosphere in the gas phase if the volumetric hydrogen content in oxygen exceeds 4%. We have developed a transient model of a multi-cell stack which can describe the operation of the electrolyzer with mixed electrolyte flows (anolyte and catholyte), separated flows, or a combination thereof (dynamic switching). This is a major extension of the steady-state model developed by Haug et al. (International Journal of Hydrogen Energy, 2017, 42, 15,689–15707). In sharp contrast to the steady-state model by Haug et al., the transient

Transient modelling
Potassium hydroxide

model can calculate the gas crossover as the operating conditions (*e.g.* electrolyte flow cycles) dynamically change in time. Depending on the size of the stack and the separator tanks, the model estimates different rates for impurities to build up. The transient model is validated using independent experimental results by Haug et al. and Brauns et al. (Electrochimica Acta, 2022, 404, 139,715) The results show that the dynamic model can follow experimental results for fluctuating current densities for a period of several days. We found that the dynamic response and transition time to steady state depend significantly on the geometrical volume of the gas separators with respect to the single-cell stack. For a multi-cell stack, we find that the impurities build-up faster when increasing the number of cells in the stack. This model serves as a tool for sizing and process management of the electrolyzer system and the separator tanks especially with respect to explosion safety.

Introduction

Reducing greenhouse gas (GHG) emissions across different industries is one of the greatest challenges of the 21st century [1,2]. GHG emissions trap the heat in the atmosphere and have a negative impact on climate change [2,3]. The main contributors to current GHG emissions are carbon dioxide (CO_2), methane (CH_4) and Nitrous Oxide (N_2O). An option to reduce the GHG emissions can be the use of green hydrogen [4,5]. The word "green" implies that the electricity used for hydrogen production is originated from renewable sources *e.g.* wind and solar [4]. Water electrolysis has become significantly popular as a way to decarbonize industrial processes and different sectors [6]. Popular research topics in the recent years include simulation, operation and design optimization, coupling to renewable sources, storage technologies, economics, storage, etc. An overview of these research topics in the recent years is provided in Ref. [6]. Water electrolysis involves splitting water using electrochemical principles into its building blocks; hydrogen and oxygen.

Alkaline water electrolysis (AWE) is the most mature and commercially available technology since 1902 [7]. The first AWE was demonstrated by Van Troostwijk and Deinman in 1789 [8]. The electrolysis cell consists of two porous electrodes, namely the anode and the cathode. The electrodes are immersed in a strong liquid alkaline electrolyte which is either potassium hydroxide (KOH) or sodium hydroxide (NaOH). The electric conductivity of the electrolyte solution allows charge transfer (electricity) within the aqueous electrolyte solution. To avoid the mixing of the evolved gases at the anode and the cathode (gas crossover), a separator is placed between the cathodic and anodic compartments. The efficiency and performance of the cell depends on the geometry, electrode and separator materials, electrolyte flow rates, etc. [9]. In typical alkaline technology, the separator can significantly reduce the gas crossover however it cannot completely eliminate it. The gas crossover takes place when the produced hydrogen at the cathodic half-cell permeates to the anodic half-cell, or the produced oxygen at the anodic half-cell permeates to the cathodic half-cell [10].

The cathodic and anodic half-cell reactions are

$$2H_2O + 2e^- \rightarrow 2OH^- + H_2 \tag{R1}$$

$$2OH^- \rightarrow 0.5O_2 + H_2O + 2e^- \tag{R2}$$

and the overall reaction is:

$$H_2O \rightarrow H_2 + 0.5O_2 \tag{R3}$$

When direct current (DC) is supplied to the electrolysis cell, H_2O is reduced at the cathode, and H_2 with OH^- ions are produced. This reaction (R1) is often called the hydrogen evolution reaction (HER). In the anodic half-cell (R2), OH^- ions are oxidized, resulting in oxygen and water molecules. This reaction is often called the oxygen evolution reaction (OER).

Green hydrogen production is bound by fluctuating electricity production from wind and solar energy [10,11]. Fluctuating load profiles of wind turbines and photovoltaic systems lead to electrolyzers operating on partial load relative to the nominal load [10]. A technical evaluation of the flexibility of different electrolysis systems is provided in Ref. [12]. The nominal load is typically referred to a current density in a cell resulting in an efficiency of 70% based on the lower heating value of hydrogen [10]. The partial load range of conventional AWE is limited to 10%–40% [13]. Reducing the partial load results in an increase in gas impurities at both half-cells [13–15]. It is important to note that the frequency at which the electrolyzer is operated at partial load depends on the number of electrolyzers installed, the total capacity of the stacks, the nominal power of the wind and solar, and whether there is any battery energy storage systems installed before the electrolyzer. The implications of coupling fluctuating and highly intermittent renewable energy sources and dynamic AWE operation are summarized in Ref. [16]. An example of a variable load coupled to a pressurized alkaline electrolyzer with a capacity of 250 kW is studied in Ref. [17]. Gas crossover at partial loads is critical according to explosion safety regulations [7,10,15,18]. Operating the electrolyzer above the nominal load is bounded by lifetime issues [10,13,15]. Another important parameter for an electrolyzer is the maximum current, which depends on several factors including current efficiency, energy efficiency, material limitations, etc. Determining the maximum current for a specific electrolyzer is however beyond the scope of this work.

Different phenomena contribute to gas crossover including: *(1) diffusive mass transfer*: the dissolved species (oxygen and hydrogen) can diffuse through the separator to the opposite half-cell, *(2) convective mass transfer*: mass transfer across the separator due to a pressure differential between the cathodic and anodic half-cells, *(3) mixing electrolyte flows from anodic and cathodic separator tanks (anolyte and catholyte) entering the electrolyzer.* Anolyte returning from the separator tank is saturated with oxygen, while catholyte flow from the separator tank is saturated with hydrogen. Mixing anolyte and catholyte flows leads to dissolved hydrogen and oxygen entering the anodic and cathodic half-cells, respectively [19]. It was demonstrated using experiments [15,20] and modelling [14] that electrolyte mixing outweighs diffusive mass transfer and convective mass transfer. The contribution of diffusive mass transfer increases with increasing temperature, decreasing separator thickness, and lower electrolyte flow rates [19]. Uncontrolled gas crossover especially during the partial-load operation of the electrolyzer may lead to an explosive atmosphere in the separator tanks. The hydrogen-oxygen mixture can lead to spontaneous combustion if the concentration of the oxygen or hydrogen in the mixture reaches ca. 4% vol., which is the Lower Explosive Limit (LEL) [18]. The exact value of the LEL may slightly deviate from 4% depending on the operating temperature and pressure. Another disadvantage of gas crossover is the loss of hydrogen product. The amount of hydrogen entering the anodic compartment and the separator tank is usually not recovered, and it enters the atmosphere. To remove the oxygen entering the cathodic compartment or the separator tank, a catalytic reaction may be used in which part of the produced hydrogen is also used to remove the oxygen which reduces the efficiency of the electrolysis plant [21].

Haug et al. [15] proposed a dynamic method of operating the alkaline electrolyzer to reduce the gas crossover especially at low current densities. In this method, the system is operated in a so-called "mixed" and "separated" electrolyte flows. A schematic representation of mixed and separated electrolyte flow cycles is shown in the simplified process flow diagram in Fig. 1. Operating in mixed flow includes mixing of anolyte and catholyte at the inlet of the electrolyzer. When the electrolyzer is operated at 1 bar, with mixed electrolyte flows, the contribution to the gas crossover due to the pressure differential between the two-half cells is usually negligible [14]. In this case, the electrolyte mixing due to convective mass transfer, and the diffusion flux due to the difference in the concentration of species in the half-cells play a dominant role in the gas crossover [14,15,22]. The concentration gradient forms over time due to production and consumption of water in the cathodic and anodic compartments as in Reactions R1 and R2 [14]. Electrolyte mixing is required to avoid having an electrolyte concentration gradient between the cathodic and anodic half-cells [14]. Gas crossover due to electrolyte mixing is shown to have a significant contribution in the AWE [14,15,20]. When operating in separated flows, the anolyte and catholyte flows enter the electrolyzer separately, without mixing. In this way, diffusion through the separator is the predominant mechanism for gas crossover assuming equal pressures in both half cells. Dynamic operation means that the anolyte and catholyte flows are managed to be mixed or separated during electrolysis [14,15]. This leads to a decrease in gas crossover compared to operating the process fully with mixed electrolyte flows.
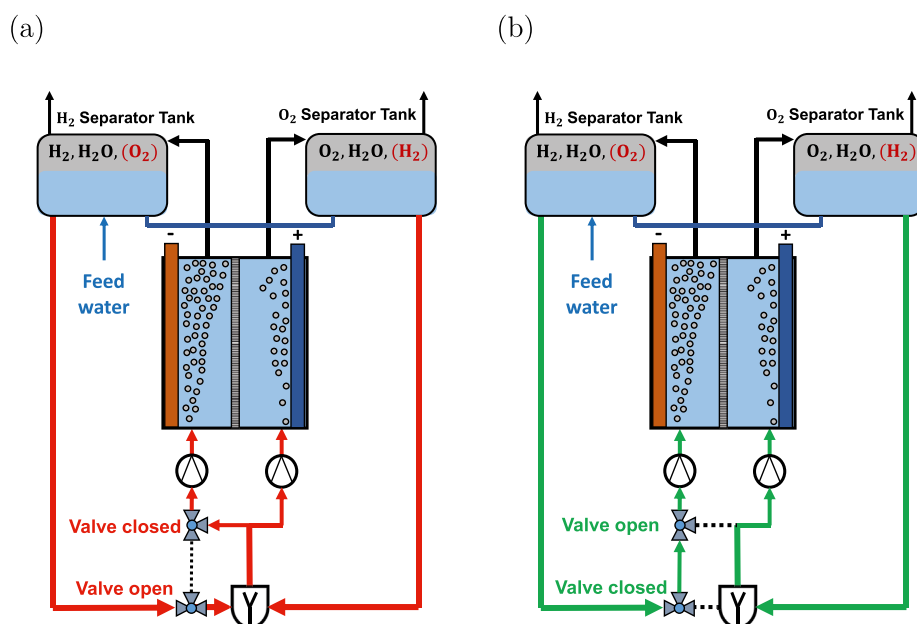
(a)   (b)

Fig. 1 − **Simplified process flow diagram of the electrolysis plant. (a) Mixed electrolyte cycles (b) Separated electrolyte cycles. In this process flow diagram, two 3-way valves are used on the cathodic side to switch between mixed and separated electrolyte flows. In principle other valve configurations are possible to achieve mixed and separated electrolyte cycles. The outlet of the cathodic separator tank contains hydrogen, water and oxygen, as impurity. The outlet of the anodic separator tank contains oxygen, water, and hydrogen, as impurity.**

Multidimensional modelling of AWEs has drawn attention of researchers in the recent years [23–27]. Lee et al. [23] have developed a three-dimensional transient model of an AWE without considering the gas crossover in the mathematical model. Cruz et al. [24] have developed a transient model to minimize the cost with respect to fluctuating electricity price. As a recommendation for future work, Cruz et al. have mentioned mixing of hydrogen and oxygen through the liquid electrolyte (which leads to crossover). Sakas et al. [25] developed a dynamic model using Simulink [28] to compute the mass flow rate of product gases and the polarization curve. This model does not consider the purity of the product gases at the outlet of the gas separators and the gas crossover mechanisms. The following studies have addressed gas crossover with different levels of rigour. Haug et al. [14] developed a steady-state model for predicting gas crossover in AWE. This model is based on a Continuous Stirred-Tank Reactor (CSTR) model for the cell. The gas crossover is computed as a function of current density, temperature, electrolyte concentration, and flow rate in the electrolyzer. The mechanisms for the gas crossover considered in this work are electrolyte mixing and diffusion through the separator. Sanchez et al. [29] developed a MATLAB [30] model where the anodic hydrogen content (due to the crossover) is calculated using semi-empirical correlations as a function of the current density. In this model, the gas crossover mechanisms are not considered in detail using physically based models. De Groot et al. [19] developed a steady-state model to compute the impurity of product gases for operating pressures up to 20 bara. In sharp contrast to the work of Haug et al. [14], the gas crossover due to differential pressure through the separator is also considered by De Groot et al. Based on the aforementioned references on gas crossover modelling, it is clear that the transient models are not thoroughly addressed in combination with gas crossover and purity of product gases. The transient model developed in this work predicts the product gas impurity using transient mass balance equations. The model can be used to calculate the impurities during start-up or shutdown time of the electrolyzer as well as steady-state operation. To make a model applicable to electrolyzers with a plurality of cells, the single cell transient model was extended to a multi-cell electrolyzer as well. As a result, the electrolyzer can operate safely without exceeding the LEL below partial-load. It should be noted that due to the CSTR model, a uniform concentration throughout the electrolysis cell is assumed, and the complex mass transfer mechanisms in the vicinity of the electrodes are lumped in the gas evolution efficiency. This makes the model robust and fast for simulation. However, for more advanced simulations, a more physically based model with more physical dimensions of the cell is recommended.

The rest of this paper is organized as follows. In Section Mathematical Model, the mathematical model developed in this work is described. The model is based on CSTR and the conservation of mass equations per species in every half-cell and in the separator tanks. Experimentally determined parameters required for optimizing the transient model are introduced in this section. These parameters include diffusion coefficients, solubilities in water and electrolyte solutions, and bubble size distributions of hydrogen and oxygen product gases. The transient model is also extended to a multi-cell stack in which the number of cells can be changed as an input parameter. An overview of mass transfer models used in this work is provided in Section Mass Transfer. In Section Simulation Details, simulation details and boundary conditions used for the single-cell and multi-cell models are explained. Simulation parameters and input data are summarized in Section Parameters. To validate the model, the same parameters as in Refs. [14,15] are used. In Section Results, the model is validated, for a single-cell stack, using experimental measurements by Haug et al. [14,15]. A sensitivity analysis is provided to study the dynamic response of the system by changing operating parameters such as temperature, liquid flow rate, mass fraction of KOH in the electrolyte solution, and the volume of the separator tanks. It is shown that the liquid flow rate, temperature and the mass fraction of KOH affect the anodic hydrogen content, while the transition time to steady-state is not significantly affected compared to changes in the volume of the separator tank. For a multi-cell model, the dynamic response of the system is studied for a fixed separator tank volume and stack sizes between 1 and 20 cells. The model shows a faster rate for building up impurities with increasing the number of cells. To avoid certain impurity thresholds (e.g., 2% vol.), one can reduce switching time between mixed and separated electrolyte cycles. It is shown that in general, a smaller switching time can be used for a larger stack. Our conclusions are summarized in Section Conclusions. We find that the model can predict the anodic hydrogen content in excellent agreement with available experimental data [15]. The present model requires the gas evolution efficiency as an input parameter which can be obtained from steady-state measurements [14,15]. The multi-cell model can be used to adjust the switching time between mixed and separated electrolyte cycles depending on the size of the separator tanks and the number of cells within the stack. The model also indicates different rates for building up impurities at startup with mixed or separated electrolyte cycles. This can be further adjusted by changing the switching time between mixed and separated electrolyte cycles.

Mathematical model

This work extends the steady-state model developed by Haug et al. [14] to a transient model which yields the production rate, anodic hydrogen content and the cathodic oxygen content, (impurities) as a function of time. In sharp contrast to Ref. [14] which models a stationary process, changes of concentrations and partial pressures of species are considered. The electrolyzer is modelled as an ideal CSTR [31] with constant temperature and concentration. Composition of product gases, which are saturated with water vapour, are sampled at the outlet of the separator tank. The model allows for simulating both mixed and separated electrolyte flows. A time-dependent input for the electrolyte flow can be used to actively switch between mixed and separated electrolyte flows. The following operating conditions can be set to calculate the composition of product gases accordingly: the current density, applied pressure, electrolyte mass fraction, liquid volumetric flow rate, liquid volume in the gas separators, and volume of the half-cells.

Transient species balance equations

In Fig. 1, simplified process flow diagram of the modelled electrolysis plant is shown. To balance the pressures between the separator tanks, one can connect the bottom of the separator tanks with a liquid level equalizer tube. This avoids a differential pressure build-up between the separator tanks and it is experimentally shown to have negligible effect on the total gas crossover [15]. Since this effect is negligible, in this work no distinction is made between partly-separated flow and separated flow, in sharp contrast to Ref. [14]. The role of the feedwater stream is to compensate for the water consumed due to gas production. To visualize the liquid and gaseous volumes inside the separator tanks, the bubbly flow is depicted as two distinct areas (ideal separation).

The transient mass balance equations, used in this work, correspond to the schematic representation shown in Fig. 1, including the electrolysis cell and two separator tanks connected to the anodic and cathodic half-cells. For setting up the mass balance equations, the electrolysis cell and the separator tanks are shown in detail in Figs. 2 and 4. The model assumes two ideal CSTR models for the cathodic and anodic half-cells. The separator tanks are also modelled based on CSTR assumptions excluding chemical reactions. It is further
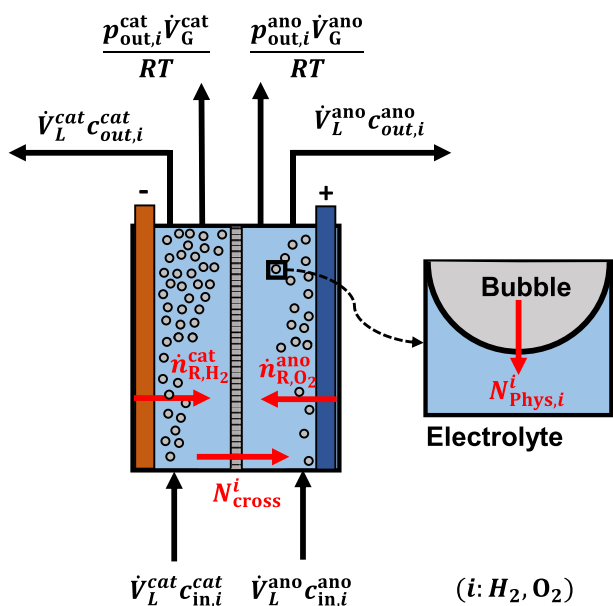

Fig. 3 – **Mass transfer mechanisms during alkaline water electrolysis. During electrolysis, product gas (H_2 or O_2) dissolves in the liquid electrolyte, in the concentration boundary layer of the electrode (flux N_D). Due to the supersaturation in the concentration boundary layer [33,35], the product gas is partly desorbed to the gas phase (flux N_G). Due to the combined effect of diffusion and convection, the rest of the product gas remains dissolved and is transferred to the electrolyte bulk (flux N_E). Due to supersaturation in the electrolyte bulk, a small amount of the dissolved product desorbs to the detached bubbles (flux N_F). The rest of the gas remains dissolved and exits the electrolysis cell. This schematic representation is based on the work of Krause and Vogt [59].**

Fig. 2 – **Illustration of different mass transfer phenomena inside the cell, included in the dynamic model. $\dot{n}_{R,i}^j$ is the reaction rate, $\dot{V}_L^j c_{in,i}^j$ is the molar flow rate of species i entering the electrolysis cell with the liquid electrolyte with a volumetric flow of $\dot{V}_L$ in compartment j. $\dot{V}_L^j c_{out,i}^j$ is the molar flow rate of species i exiting compartment j. $\frac{p_{out,i}^j \dot{V}_G^j}{R\,T}$ is the molar flow of species i in the gas phase at the outlet of compartment j, $N_{phys,i}^j$ is molar flow rate due to desorption flux between the gas phase and the electrolyte. N_{cross}^i is the molar flow rate due to the diffusion through the separator.**
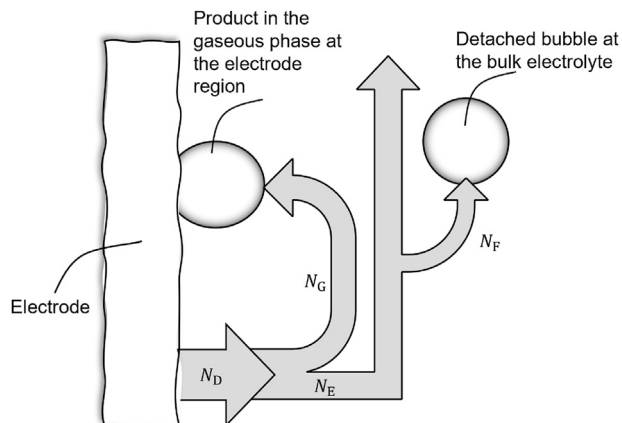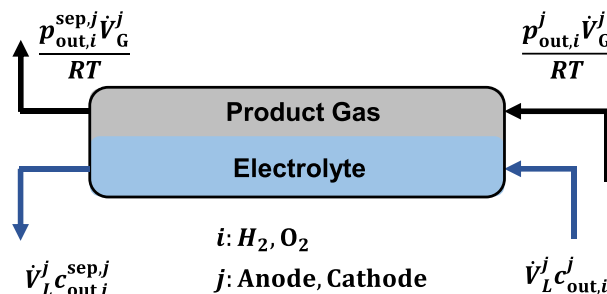

Fig. 4 – **Schematic illustration of the flows inside the separator tank. $\dot{V}_L^j c_{out,i}^j$ is the flow rate of species i entering the separator tank with the liquid electrolyte with a volumetric flow of $\dot{V}_L$ at the outlet of compartment j from the cell, $\frac{p_{out,i}^j \dot{V}_G^j}{R\,T}$ is the molar flow rate of species i in the gas phase at the outlet of compartment j from the cell, entering the separator tank. $\frac{p_{out,i}^{sep,j} \dot{V}_G^j}{R\,T}$ is the flow rate of the product gas at the outlet of the separator tank. The liquid stream at the outlet of the gas separator, $\dot{V}_L^j c_{out,i}^{sep,j}$, is recirculated.**

assumed that the composition of the electrolyte between the half-cell and the separator tank is constant. This means that the composition of the electrolyte and the product gas at the outlet of the half-cell and inlet of the separator tank are the same allowing one to couple mass balance equations for the

electrolysis cell and the separator tanks. The volumes of the interconnecting pipes are not included in the model. In the following sections, we derive the transient material balances in the electrolysis cell followed by the transient material balances in the separator tanks. All physical constants, symbols and variables are defined in the nomenclature, and are referred in the explanation of the equations as well.

Half-cells

In Fig. 2, a schematic representation of a single cell is shown consisting of cathodic and anodic half-cells separated by a separator. Each half-cell is modelled as an ideal CSTR. All mass transfer mechanisms within the half-cells and crossing the boundaries are illustrated in this figure. In the mass balance equations for the half-cells and the separator tanks, the superscript j in variable X^j refers to either the cathodic or anodic sides. This is denoted by "cat" or "ano", respectively. For thermodynamic properties such as pressure and concentration, the subscript i refers to the chemical species (H_2 or O_2). Thermodynamic properties at the inlet or outlet of the half-cells are distinguished with subscripts "in" and "out", respectively. For example, p_{out,H_2}^{ano} and c_{out,H_2}^{ano} refer to the partial pressure and concentration of hydrogen at the anodic compartment at the outlet of the half-cell, respectively. Due to the CSTR model assumption, the gas evolution at the electrolyte is instantaneous depending on the value of the current density. This means that the distribution of liquid and gas volumes within the cell is fixed per current density. The volumetric flow rates of the electrolyte and product gases corresponding to compartment j are denoted by $\dot{V}_L^j$ and $\dot{V}_G^j$, respectively. Permeation of species i across the separator is denoted as N_{cross}^i. At the liquid-gas interface in compartment j, the mass transfer rate of species i (desorption flux) is denoted as $N_{phys,i}^j$. This is shown as an inset in Fig. 2. In compartment j, the reaction of species i is denoted as $\dot{n}_{R,i}^j$. The production of hydrogen in the cathodic and anodic half-cells obeys Faraday's law [32]. Faraday's law states that the amount of substance deposited or released at the electrode is directly proportional to the quantity of charge transferred at that electrode [32].

The mass transfer mechanisms near the electrode area are shown in detail in Fig. 3. Due to the mass transfer limitations in the gas evolving electrodes [33,34], part of the product gas, N_D, is transferred to the liquid phase, N_E, and the rest, N_G, is directly transferred to the gaseous phase at the electrode region (due to supersaturation in the boundary layer) [35,36]. N_F denotes the mass transfer rate between the bulk liquid and the detached bubble bulk electrolyte. One of the parameters used in the mass balance equations is the gas evolution efficiency of hydrogen or oxygen. It is defined as the ratio between N_G and N_D denoted by $f_{G,i}$ [37]. The transient material balance for species i in the liquid phase (electrolyte) in the anodic compartment follows from:

$$\frac{dc_{out,i}^{ano}}{dt} = \frac{1}{V_{liq}^{ano}} \cdot \left[\dot{V}_L^{ano} \cdot \left(c_{in,i}^{ano} - c_{out,i}^{ano} \right) + N_{phys,i}^{ano} \cdot A_{GL}^{ano} \right.$$
$$\left. + N_{cross,i} \cdot A_d + \left(1 - f_{G,i} \right) \cdot \dot{n}_{R,i}^{ano} \right] \tag{1}$$

in which V_{liq}^{ano} is the volume of the liquid electrolyte inside the anodic half-cell, A_d is the area of the separator available for cross permeation of species, A_{GL}^{ano} is the total area at the gas liquid interface in the anodic half-cell. The reaction rate $\dot{n}_{R,i}^j$ obeys Faraday's law [32]:

$$\dot{n}_{R,i}^j = \frac{J \nu_i}{nF} A_{el} \tag{2}$$

in which the stoichiometric coefficient ν_i corresponds to Reaction R3, A_{el} is the active surface area of the electrode, and the charge transfer is $n = 2$. In Eq. 2, it is assumed that the Faradaic efficiency (current efficiency) is 100%. In a similar manner, the material balance for the dissolved species in the liquid electrolyte in the cathodic half-cell follows from:

$$\frac{dc_{out,i}^{cat}}{dt} = \frac{1}{V_{liq}^{cat}} \cdot \left[\dot{V}_L^{cat} \cdot \left(c_{in,i}^{cat} - c_{out,i}^{cat} \right) + N_{phys,i}^{cat} \cdot A_{GL}^{cat} \right.$$
$$\left. - N_{cross,i} \cdot A_d + \left(1 - f_{G,i} \right) \cdot \dot{n}_{R,i}^{cat} \right] \tag{3}$$

it is important to note that in Eqs. 1 and 3 the mass transfer flux, $N_{phys,i}^j$ is defined positive from the gas phase to the electrolyte (inset of Fig. 2). Since the electrolyte bulk is supersaturated, the mass transfer takes place from the electrolyte [34] which makes the mass transfer flux negative. The desorption mass flux is integrated over A_{GL}. The crossover flux through the separator, N_{cross}^i, is considered positive from cathode to the anode. For hydrogen, this term remains positive as cathodic bulk concentration of hydrogen is higher compared to the anodic half-cell. For oxygen, the crossover flux takes place from the anodic half-cell to the cathodic half-cell making N_{cross,O_2} negative.

For the material balance in the gas phase, it is assumed that the gas phase obeys the ideal gas law. This is justified due assuming atmospheric operation of the electrolyzer. At higher pressures, fugacity coefficients can be used to correct for non-idealities in the gas phase [38,39]. The material balance of gaseous species i in compartment j follows from:

$$\frac{dp_{out,i}^j}{dt} = -\frac{\dot{V}_G^j}{V_{gas}^j} \cdot p_{out,i}^j - \frac{R \cdot T}{V_{gas}^j} \cdot \left(N_{phys,i}^j \cdot A_{GL}^j - f_{G,i} \cdot \dot{n}_{R,i}^j \right) \tag{4}$$

in which $\dot{V}_G^j$ is the total volumetric flow rate of the product gas at the outlet of the half-cell j, V_{gas}^j is the volume of the product gas in the half-cell. R is the universal gas constant. For species i, Eq. 4 is coupled to Eqs. 1 and 3 using $N_{phys,i}^j$ and $f_{G,i}$ in the anodic and cathodic compartments. Note that the flow rates $\dot{V}_L^j$ and $\dot{V}_G^j$ are determined at the outlet of the electrolysis cell and not in the separator tanks.

Separator tanks

In Fig. 4, a schematic representation of the gas separator tank is shown. Two separator tanks are used for cathodic and anodic half-cells each. The liquid levels in both separator tanks are assumed to be equal and steady in time. This is equivalent to the liquid level equalizer in the system [14]. Similar to the electrolyzer cell, the gas separators are also modelled as CSTR ideal reactors with the distinction that no

chemical reaction takes place. The concentration of species i in the separator tank connected to the half-cell j is denoted as $c_{out,i}^{sep,j}$. In the separator tanks, no additional mass transfer between the liquid electrolyte and the gas phase is considered. It is further assumed that only the liquid electrolyte is directed back to the electrolysis cell, and the product gases exit the electrolysis plant at the outlet of the separator tanks. It is important to note that gaseous products in both anodic and cathodic compartments contain impurities. This means presence of oxygen in the hydrogen separator tank and oxygen in the hydrogen separator tank.

Mass balance equations for the separator tank are essential for transient modelling of gas impurities. As it will be shown in Section Results, the volume of the liquid electrolyte which is related to the size of the separator tank affects the time in which gas impurities reach steady state values. This is in sharp contrast to the steady-state model by Haug et al. [14] in which the physical volume of gas separator tank is not considered to calculate the impurities at steady-state conditions. The transient mass balance of species i in the separator tank of compartment j follows from:

$$\frac{dc_{out,i}^{sep,j}}{dt} = \frac{\dot{V}_L^j}{V_{liq}^{sep,j}} \cdot \left(c_{out,i}^j - c_{out,i}^{sep,j} \right) \tag{5}$$

in which $c_{out,i}^{sep,j}$ is the concentration of species in the separator tank, connected to compartment j. It is important to note that $c_{out,i}^j$ is the concentration of species i at the inlet of the separator tank which is equal to the concentration of species i at the outlet of the half-cell j. For every half-cell, Eqs. 1, 3 and 5 are coupled using the species concentrations and volumetric flow rate of the electrolyte. The material balance for the gaseous species i, in the gas separator connected to compartment j:

$$\frac{dp_{out,i}^{sep,j}}{dt} = \frac{\dot{V}_G^j}{V_{gas}^{sep,j}} \cdot \left(p_{out,i}^j - p_{out,i}^{sep,j} \right) \tag{6}$$

in which $p_{out,i}^{sep,j}$ is the partial pressure of species i in the separator tank. $p_{out,i}^j$ is the partial pressure of species i at the inlet of the separator tank which is equal to the partial pressure of species i at the outlet of the half-cell. Note that Eq. 6 is directly coupled with Eq. 4. Eqs. (1)–(6) are in total 16 coupled transient mass balance equations with 16 unknowns.

The impurity of the product gas in the anodic separator tank is the amount of H_2 in O_2. The impurity can be calculated as the mole fraction of gaseous H_2 without taking into account water vapour. This definition is consistent with the definition in Refs. [14,15] which is also used for model validation.

$$y_{H_2} = \frac{p_{out,H_2}^{sep,ano}}{p_{out,H_2}^{sep,ano} + p_{out,O_2}^{sep,ano}} \tag{7}$$

The impurity of the product gas in the cathodic separator tank is the amount of O_2 in H_2 which follows from:

$$y_{O_2} = \frac{p_{out,O_2}^{sep,cat}}{p_{out,H_2}^{sep,cat} + p_{out,O_2}^{sep,cat}} \tag{8}$$

When fitting the model to experimental data (measured impurities), it is important to distinguish between the measurements at the exit of the cell, and the measurements at the exit of the separator tanks. Measuring the impurities at the exit of the separator tanks includes the additional mass transfer between the gas and liquid phase within the separator tank. In sharp contrast, when impurities are measured after the cell outlet, the compositional changes due to the additional mass transfer in the separator tanks are excluded.

It is well-known that crossover of hydrogen to the anodic compartment is larger compared to the crossover of oxygen to the cathodic compartment [14,15,22]. This means that during operation of the electrolyzer, y_{H_2} is normally the first to cross the explosion safety limit of 4%. This is mainly due to the higher diffusion of hydrogen in the electrolyte mixture and lower production of oxygen at the anodic content with respect to hydrogen production (Eqs. R1 and R2). Therefore, considering the anodic hydrogen content is sufficient for the safety limit.

Mass transfer

The desorption flux $N_{phys,i}^j$ is the mass transfer rate of species i between the liquid electrolyte and the product gases in compartment j. Here, film theory is used to model the desorption flux [40,41]. Adjacent to the interface of the liquid and gas phase, a thin layer of liquid (film) is considered with the thickness δ [42]. This can be extended to two films in series including a gas film adjacent to the liquid film. Assuming negligible mass transfer resistance at the gas interface, the mass flux of species is governed by the liquid film [14]. By applying Fick's law of diffusion, the desorption flux is obtained from:

$$N_{phys,i}^j = k_{L,i}^j \cdot \left(c_i^{*,j} - c_{out,i}^j \right) \tag{9}$$

in which $c_i^{*,j}$ is the solubility of species i in liquid film (electrolyte) in equilibrium with the product gas in compartment j. $k_{L,i}^j$ is the mass transfer coefficient in the liquid film obtained from the ratio between the diffusion coefficient in the liquid film and the liquid film thickness: $\frac{D}{\delta_L}$. This ratio is normally unknown [40], however, the mass transfer coefficient can be modelled by applying empirical Sherwood correlations [14]. The equilibrium concentration $c_i^{*,j}$ in aqueous KOH solution is expressed as a function of the partial pressure of species i in the gas phase, $p_{out,i}^j$. First, the solubilities of hydrogen and oxygen in pure water are related to their partial pressures by Henry's law [43]. Second, solubilities of hydrogen and oxygen in aqueous KOH solutions are obtained using the Sechenov equation [14,44,45]. Combining Henry's law and the Sechenov equation leads to the following:

$$c_i^{*,j} = \frac{\rho_{H_2O} \cdot p_{out,i}^j}{M_{H_2O} \cdot 101325 \cdot H_i \cdot 10^{K_{S,i} \cdot w_{KOH}}} \tag{10}$$

in which ρ_{H_2O} is the density of pure water in [kg m^{-3}] [46], M_{H_2O} is the molar mass of water in [g mol^{-1}], H_i is the Henry's constant in [atm], and $K_{S,i}$ is the Sechenov constant of species i, and w_{KOH} is the KOH mass fraction. For the calculation of $k_{L,i}^j$ the reader is referred to Refs. [47,48].

Permeation flux through the separator, $N_{cross,i}$, is driven by diffusion and differential pressure. Due to the atmospheric operation of the cell, the differential pressure between the half-cells is considered negligible in this model, and the permeation flux is controlled by the concentration gradient of species in the anodic and cathodic half-cells. Using Fick's law, the permeation flux is obtained from:

$$N_{cross,i} = \frac{D_i^{eff}}{d_d} \bullet \left(c_{out,i}^{cat} - c_{out,i}^{ano} \right) \tag{11}$$

where d_d is the thickness of the separator, and D_i^{eff} is the effective diffusion coefficient of species i. The effective diffusion coefficient is a function of the molecular diffusion of species i in the liquid electrolyte [49], porosity, ϵ, and tortuosity, τ, of the separator.

$$D_i^{eff} = D_{i,\theta} \frac{\epsilon}{\tau} \tag{12}$$

in which $D_{i,\theta}$ is molecular diffusion coefficient of hydrogen or oxygen. Molecular diffusion data can be found using experimental data [14,49] or advanced simulation techniques such as molecular simulations [50].

Simulation details

Boundary conditions for mixed and separated flows

Simulations of the electrolysis plant can be performed with separate electrolyte flows, mixed electrolyte flows, or a combination thereof as a function of time. For every case, the boundary conditions of the electrolysis cell can be defined. For both mixed and separated flows, it is assumed that no product gases are recirculated throughout the system. Therefore, the inlet volumetric flow rate is gas-free. For mixed flows, the volumetric flow of the electrolyte entering the electrolysis cell follows from:

$$\dot{V}_{mix} = \dot{V}_L^{ano} + \dot{V}_L^{cat} \tag{13}$$

it is assumed that the mixer distributes the flow equally between the half-cells. The concentration of species in the volumetric flows correspond to the outlet of the hydrogen and oxygen separator tanks, $c_{out,i}^{sep,j}$. Assuming ideal mixing of the anolyte and the catholyte before the inlet of the electrolysis cell (see Fig. 1), the inlet concentration in both half-cells is obtained from:

$$c_{in,i}^j = c_i^{mix} \tag{14}$$

The dissolved mixed concentration c_i^{mix} can be found by applying a mass balance for the ideal mixer before the inlet of the electrolysis cell (see Fig. 1) for each species i.

$$c_{in,i}^j = c_i^{mix} = \frac{\dot{V}_L^{ano} \bullet c_{out,i}^{sep,ano} + \dot{V}_L^{cat} \bullet c_{out,i}^{sep,cat}}{\dot{V}_{mix}} \tag{15}$$

For separated flows, the concentration of the species at the inlet of the half-cells, $c_{in,i}^j$, is equal to the liquid concentration of the species at the outlet of the gas separators, $c_{out,i}^{sep,j}$. In this

model, no additional mass transfer is considered for the interconnecting pipes. This means:

$$c_{in,i}^{ano} = c_{out,i}^{sep,ano} \tag{16}$$

Switching between mixed and separated electrolyte flows in Eqs. 14 and 16 can be performed dynamically as a function of time during the simulation.

Extending the model to a n-cell stack

In the *n*-cell stack, every cell is modelled in a similar manner as explained above. A schematic representation of the *n*-cell stack is shown in Fig. 5. The only difference is that two ideal manifolds are placed at the inlet and outlet of the stack. The manifold is used only for flow distribution at the inlet of the stack and collecting flows from the output of the stack. On the hydrogen side, the manifold distributes the catholyte flow from the pump equally between the cathodic half-cells. On the oxygen side, the anolyte flow is also equally distributed between the anodic half-cells. No mixing between the anolyte and catholyte flows takes place in the manifold. At the outlet, the manifold collects the bubbly catholyte flow from cathodic
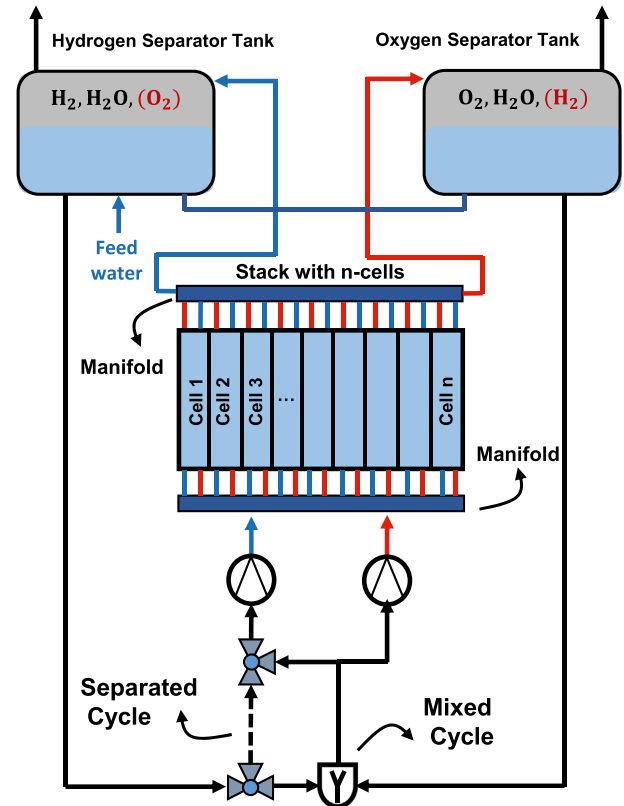

Fig. 5 – Schematic representation of the n-cell electrolyzer corresponding to the extended transient model. Manifolds distribute the flow between the anodic and cathodic half-cells without any mixing. The manifold at the outlet of the stack collects the bubbly anolyte flow directed to the anodic separator tank. The bubbly catholyte flow is directed to the cathodic separator tank.

Property	Value	Units	Reference
γ	0.08267	N m^{-1}	[54]
f_{G,H_2}	0.68	–	[14]
f_{G,O_2}	1	–	[14]
p_{H_2O}	27583.85058	Pa	[14]
d_b^{cat}	0.000157	m	[14]
A_{GL}^{ano}	2.95850	m^2	[14]
A_{GL}^{cat}	2.97927	m^2	[14]
$\epsilon_{g,out}^{ano}$	0.14631	–	[14]
$\epsilon_{g,out}^{cat}$	0.22969	–	[14]
$D_{H_2,\theta=80}$	$5.58823 \cdot 10^{-9}$	m^2 s^{-1}	[49]
$D_{O_2,\theta=80}$	$1.68098 \cdot 10^{-9}$	m^2 s^{-1}	[49]
μ_L	0.00087	Pa s	[14]
ρ_L	1276.48135	kg m^{-3}	[55]
ρ_{H_2O}	971.79778	kg m^{-3}	[46]
H_{H_2}	71661.82123	atm	[43]
H_{O_2}	69577.49411	atm	[43]
K_{S,H_2}	3.14	–	[14]
K_{S,O_2}	3.96	–	[14]
k_{L,H_2}^{ano}	0.00042	m s^{-1}	[14]
k_{L,H_2}^{cat}	0.00033	m s^{-1}	[14]
k_{L,O_2}^{ano}	0.00020	m s^{-1}	[14]
k_{L,O_2}^{cat}	0.00016	m s^{-1}	[14]

half-cells and directs the flow to the hydrogen separator tank. In a similar manner, the manifold at the outlet collects the bubbly anolyte flow from anodic half-cells and directs the flow to oxygen separator tank.

Parameters

To verify the transient model, a dynamic simulation of the electrolyte cycles is performed corresponding to the operating conditions of the experiment in Ref. [15]. In this work, no additional fitting parameters are used other than the physical parameters reported by Haug et al. [14,15] The applied current

density equals $J = 1\,kA\,m^{-2}$, the applied temperature is $T = 80\,°C$, the applied pressure is $p^{ano} = p^{cat} = 1\,bar$, the liquid volumetric flow rates are $\dot{V}_L^{ano} = \dot{V}_L^{cat} = 0.33\,L\,min^{-1}$, and the KOH mass fraction of the liquid electrolyte is $w_{KOH} = 32\,wt\%$. An overview of the operating conditions are provided in Table 1. The design characteristics of the electrolysis plant are summarized in Table 2. In the following, details on calculating simulation parameters are provided.

Gas evolution efficiency

The gas evolution efficiency is a parameter which needs to be fitted to optimize the performance of the model. In this work, the gas evolution efficiency (defined in Section Half-Cells) is adopted from the experimental work of Haug et al. [14]. This is because the experimental results by Haug et al. in Ref. [15] are used for model validation. The same experimental setup is also used by Brauns et al. [13] for experiments at 7 bar with a variable current input during 72 h. The experimental results by Brauns et al. are also used for model validation, using the same gas evolution efficiency. From Ref. [14], the gas evolution efficiency of hydrogen in the cathodic half-cell is defined as:

$$f_{G,H_2} = 0.25744 \cdot \left(J/A\,m^{-2}\right)^{0.14134} \tag{17}$$

where J is the applied current density. The gas evolution efficiency of oxygen at the cathodic half-cell is considered equal to unity [14]. The gas evolution efficiency in Ref. [14] is calculated based on the gas impurities measured at the exit of the gas separators. Therefore, any additional mass transfer in the gas separators is lumped in practice into the gas evolution efficiency term [14,15].

In mass balance equations, the liquid and gaseous volumes inside the half-cells, V_{liq}^j and V_{gas}^j, and the gas separators $V_{liq}^{sep,j}$ $V_{gas}^{sep,j}$ are required as input parameters. To obtain these parameters, the bubble size distribution, gas holdup and pressure inside each half-cell are required. The diameter of the produced bubbles in the half-cell j is obtained experimentally [14]:

$$d_b^{cat} = 593.84 \cdot 10^{-6} \cdot (1 + 0.2J)^{-0.25} \tag{18}$$

Table 2 – Design characteristics of the experimental electrolysis setup of Haug et al. [15].

Property	Symbol	Value	Units
Electrode area	A_{el}	150	cm^2
Separator area	A_d	232	cm^2
Separator thickness	d_d	500	μm
Separator porosity	ϵ	0.55	–
Separator tortuosity	T	3.14	–
Half-cell volume	V_{hcell}	$0.16 \times 0.015 \times 0.145$	m^3
Liquid volume in the gas separator j	$V_{liq}^{sep,j}$	1.2	L
Liquid volume in the anodic half-cell	V_{liq}^{ano}	29.87×10^{-5}	m^3
Liquid volume in the cathodic half-cell	V_{liq}^{cat}	26.97×10^{-5}	m^3
Gaseous volume in the anodic gas separator	$V_{gas}^{sep,ano}$	1.55	L
Gaseous volume in the cathodic gas separator	$V_{gas}^{sep,cat}$	1.52	L
Gaseous volume in the anodic half-cell	V_{gas}^{ano}	4.93×10^{-5}	m^3
Gaseous volume in the cathodic half-cell	V_{gas}^{cat}	7.83×10^{-5}	m^3

in which the current density is in units of [kA m^{-2}], and the bubble diameter is in units of [m]. The diameter of oxygen bubbles in the anodic half-cell is considered constant at $d_{\mathrm{b}}^{\mathrm{ano}} = 10^{-4}$. The bubbles which are considered monodisperse and perfectly spherical, and coalescence effects are not considered. The total gas volume in compartment j, V_{gas}^{j}, is obtained using [14].

$$V_{\mathrm{gas}}^{j} = \epsilon_{\mathrm{g,out}}^{j} \cdot V_{\mathrm{b}}^{j} \cdot \frac{p^{j}}{p_{\mathrm{tot}}^{j}} \tag{19}$$

in which $\epsilon_{\mathrm{g,out}}^{j}$ is the gas hold-up fraction at the outlet of the half-cell, and V_{b}^{j} is the volume of a single bubble. The gas holdup is required for the calculation of the total gaseous volume within the anodic or cathodic compartment. Eq. 18 can be used to compute the volume of the hydrogen bubble, and for the oxygen bubble $d_{\mathrm{b}}^{\mathrm{ano}} = 10^{-4}$ is used. In Ref. [14], the gas hold-up fraction is obtained experimentally using

$$\epsilon_{\mathrm{g,out}}^{j} = X_1 - X_2 \cdot X_3^{J} \tag{20}$$

where J is the current density in [kA m^{-2}] and the coefficients X_1, X_2 and X_3 are given in Table 3 for the anodic and cathodic half-cells. In Eq. 19, p_{tot}^{j} is the total pressure of the cell, which is the sum of the partial pressures of the produced gases and water vapour:

$$p_{\mathrm{tot}}^{j} = p_{\mathrm{out,H_2}}^{j} + p_{\mathrm{out,O_2}}^{j} + p_{\mathrm{H_2O}} \tag{21}$$

Hydrogen and oxygen produced in the cell are saturated with water [38,39,50,51]. The water vapour partial pressure pH$_2$O can be calculated based on the work by Balej et al. [52]. Alternatively, total pressure of the cell is the sum of the atmospheric pressure p^{j} on the liquid electrolyte, exerted due to the connection of the separator tank to the atmosphere, and overpressure due to surface tension of the produced gas bubbles [14]. This is modelled using the Young-Laplace equation [53].

$$p_{\mathrm{tot}}^{j} = p^{j} + \gamma \frac{4}{d_{\mathrm{b}}^{j}} \tag{22}$$

The second term on the right hand side is the pressure contribution due to surface tension as a function of the bubble diameter. The surface tension γ in the liquid electrolyte can be calculated as a function of the applied temperature and KOH mass fraction [54]. Considering the volume of the half-cell, and the gas volume from Eq. 19, the liquid volume in the half-cell is calculated using

$$V_{\mathrm{liq}}^{j} = V_{\mathrm{hcell}} - V_{\mathrm{gas}}^{j} \tag{23}$$

Based on the gas volume from Eq. 19, the area of the gas-liquid interface follows from Ref. [14].

$$A_{\mathrm{GL}}^{j} = \frac{V_{\mathrm{gas}}^{j}}{V_{\mathrm{b}}^{j}} \cdot S_{\mathrm{b}}^{j} \tag{24}$$

in which S_{b}^{j} is the surface area of a single bubble in the half-cell j which is obtained using:

$$S_{\mathrm{b}}^{j} = \pi \cdot \left(d_{\mathrm{b}}^{j} \right)^{2} \tag{25}$$

The total volume of the gas phase on anodic or cathodic side is the sum of the gas volume in the separator tank, and the gas volume in the half-cell. To validate the model, the total volume of $V_{\mathrm{gas}}^{\mathrm{tot},j} = 1.6$ L of Ref. [14] is considered here to compute the volume of the separator tank. The volume of the liquid in the separator tank in each compartment is $V_{\mathrm{liq}}^{\mathrm{sep},j} = 1.2$ L.

For the calculation of the Sherwood number and the mass transfer coefficient $k_{\mathrm{L},i}^{j}$, the density of the liquid electrolyte ρ_{L} is obtained from the work of Gilliam et al. [55], as a function of the operating temperature and KOH mass fraction in wt%. The dynamic viscosity, μ_{L}, is obtained from Ref. [14] and is calculated in units of [Pa s].

The system of ordinary differential equations (ODEs) (Eqs. (1)–(6)) are solved using the SciPy package [56]. The solver requires an initial condition for the set of ODEs. When starting up the electrolyzer at $t = 0$, the initial values of the unknown terms are considered zero. This typically means that the alkaline water electrolyzer is inactive when it starts up. In principle other operating conditions can be selected as initial conditions for the solver.

Results

The results obtained from the dynamic model developed in this work are compared to the experimental results published by Haug et al. [15] and by Brauns et al. [13] with the same operating conditions and design characteristics. The input properties for the operating conditions of the experimental dynamic switching of electrolyte cycles are listed in Table 1. The design characteristics of the electrolysis cell are listed in Table 2. Subsequently, a sensitivity analysis is performed to investigate the dynamic response of the system by changing operating conditions and design characteristics.

Validation

In Fig. 6, the mole fraction of anodic hydrogen in oxygen (impurity) is shown as a function of time. Markers indicate the experimental results reported by Haug et al. [15]. The solid line indicates the results obtained from the dynamic model developed in this work. The computed impurity with mixed electrolyte flows is shown with red solid lines, and the green lines indicate the impurity computed with separated electrolyte flows. In a similar manner, red markers indicate experimentally measured impurities obtained from mixed electrolyte flows. Green markers correspond to experimentally measured impurities obtained from separated electrolyte flows. The dashed line is the average anodic hydrogen content obtained from the model during the dynamic switching. The

Table 3 — Parameters used in Eq. (20) to compute the gas hold-up as a function of the current density J in kAm^{-2} [14].

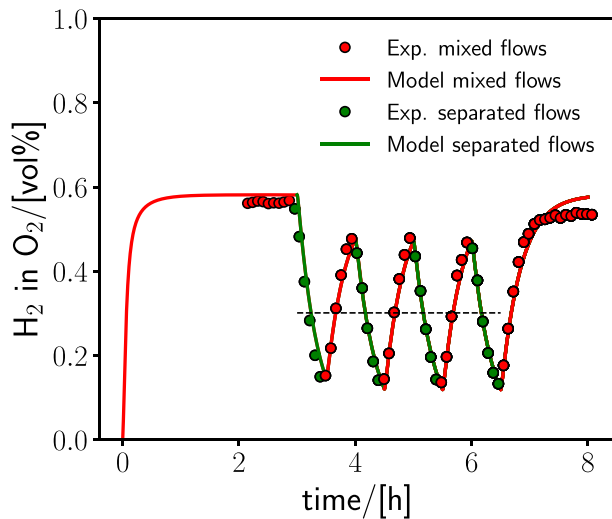| Compartment	X_1	X_2	X_3
Anode	0.59438	0.59231	0.75647
Cathode	0.76764	0.73233	0.73457

Fig. 6 – **Validation of the dynamic switching model with the experimental results of Haug et al. [15]. After a startup time of 2.5 h using mixed electrolyte cycles, switching between mixed and separate electrolyte cycles takes place every 30 min. Markers indicate the experimental results by Haug et al. [15], the results obtained from the dynamic model with solid lines. The red line and the red markers indicate mixed electrolyte cycles. The green lines and the green markers indicate separated electrolyte cycles. The dashed line is the average anodic hydrogen content obtained from the model during the dynamic switching which equals $y_{H_2}^{avg.mod} = 0.29$ vol%. The average anodic hydrogen content reported by Haug et al. [14] equals $y_{H_2}^{avg} = 0.31$**

average anodic hydrogen content reported by Haug et al. [14] equals $y_{H_2}^{avg} = 0.31$ vol%, and the model predicts a value of $y_{H_2}^{avg.mod} = 0.29$ vol%. As it is observed in Fig. 6, the anodic hydrogen content fluctuates which is the result of the switching between mixed and separated electrolyte flows (red and green) every 30 min. Using Faraday's law, it is straightforward to show that the water consumption during the experiment is in order of milliliters compared to the volume of the separator tanks. For example, running the setup for 30 min at $I = 12$ A leads to the consumption of around 2 g of water (using Faraday's law) which is around 2 mL. This is negligible compared to the total volume of the liquid electrolyte in the system. Therefore, it is assumed that the concentration of the electrolyte is constant during the experiment.

During the system startup, 0 h $\leq t_{tot} \leq 3$ h, electrolyte flows are mixed until steady state is reached in terms of the anodic hydrogen content. In this time interval, the boundary condition of Eq. 14 is used. When 3 h $< t_{tot} \leq 3.5$ h, the electrolyte flows are circulated separately (separated mode). In this case, Eq. 16 is used as the boundary condition. When switching to separated mode, an instantaneous drop in the anodic hydrogen content is observed based on the model which is in excellent agreement with the results obtained by Haug et al. [14]. Based on the material balances (Eqs. (1)–(6)), the gas crossover in separated mode is only due to the diffusion through the separator. After 30 min, the partly separated flow

changes to mixed mode in which the anolyte and catholyte flows are mixed again. The boundary conditions of the mixed mode are used as in Eq. 14. As a result, the anodic hydrogen content starts increasing due to electrolyte mixing before the entrance of the electrolysis cell. The continuous switching between the mixed mode and the separated mode takes place every 30 min, until $t_{tot} = 6.5$ h. At this point, the mixed mode boundary conditions are imported into the model, and the system approaches its steady-state anodic hydrogen content until $t_{tot} = 8$ h.

It is observed that the model predicts the experimental steady-state anodic hydrogen content until $t_{tot} = 3$ h. Combining the mixed and separated mode of electrolyte flows leads to a decrease in the anodic hydrogen content. In Fig. 6, it is shown that the results from the model follow this decrease successfully. When $t_{tot} = 3.5, 4.5, 5.5, 6.5$ h, the model predicts a slightly lower anodic hydrogen content at the end of the separated mode. The underestimation of the anodic hydrogen content can be due to a large concentration gradient across the separator. Due to the CSTR model and the uniform concentration throughout the half-cell, the model cannot capture phenomena of local supersaturation. However, the maximum anodic hydrogen content is in excellent agreement with the experimental results at $t_{tot} = 4, 5, 6$ h. The experimental impurities reported by Haug et al. [14] are slightly lower compared to the steady-state results obtained from the model for $t > 6.5$ h.

Overall, the dynamic model sufficiently validates the experimental results in Ref. [15] and captures the sinusoidal response during the dynamic switching of electrolyte cycles. The average anodic hydrogen content, which is calculated by the model, slightly deviates from the experimental average value. Despite the lower anodic hydrogen content which is predicted from the model when switching occurs from the separated to the mixed mode, the results from the model and the experiment are in excellent agreement.

Using the same experimental setup as used by Haug et al. [15], Brauns et al. [13] implemented a synthetic current density profile, representing fluctuations from PV and wind power, to evaluate how the anodic hydrogen content dynamically changes with time for a period of 72 h. This allows the use of the same gas evolution efficiency as in Ref. [14]. In addition to the fluctuating current, the experiment is performed at a pressure of 7 bar, which differs from the previous experiment by Haug et al. which was performed at atmospheric pressure [14,15]. The synthetic current density of Ref. [13] was digitized as an approximation as the exact raw data were not reported. This is shown in Fig. 7 (a). The model developed in this work was tested and compared to the reported experimental data from Ref. [13], and the results are shown in Fig. 7(b). The experimental results are shown with triangles and circles for dynamic switching and mixed electrolyte cycles, respectively. The model uses 10 input signals per hour as an approximation for the signal of Ref. [13]. The dotted line (black) is the impurity obtained from the model with dynamic switching every 2 h. Although a good agreement is already observed between the model and the experimental results, near perfect agreement is obtained by considering additional crossover mechanism contribution due to the differential pressure between the half-cells [22] (continuous cyan line):
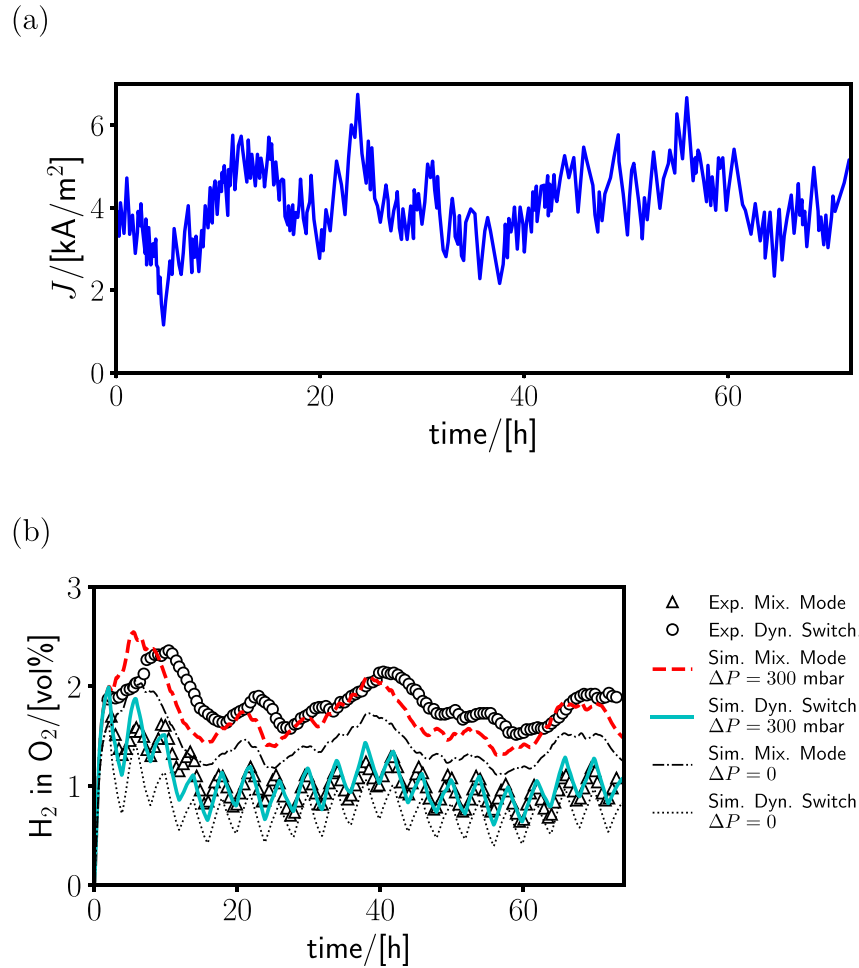
Fig. 7 — (a) Synthetic current density profile representing fluctuations from wind power for a period of 72 h as reported by Brauns et al. [13], with the experimental setup of Haug et al. [15]. (b) Validation of the dynamic model, using the data from subfigure (a), by comparing the calculated anodic hydrogen content to the experimental impurities of Brauns et al. [13]: triangles are the experimental impurities measured during dynamic switching. Circles are the experimental data measured during electrolyte mixing. The continuous cyan line corresponds to the result obtained from the model including crossover permeation due to the differential pressure between the half-cells (300 mbar). The dotted line is the obtained result from dynamic switching assuming no pressure differential between the half-cells. The red dashed line is the obtained result from the model with mixed electrolyte cycles with the pressure differential between the half-cells. The dashed dotted line are the impurities obtained considering no pressure differential during the mixed mode. (For interpretation of the references to color in this figure legend, the reader is referred to the Web version of this article.)

$$N_{H_2}^{dp} = \frac{K_{sep}}{\eta} S_{H_2} p_{H_2}^{cat} \frac{\Delta P}{d_{sep}}$$ (26)

in which ΔP is the differential pressure between the cathodic and the anodic half-cells. The permeability of the Zirfon separator is estimated as 2×10^{-16} from Ref. [22]. The implementation of Eq. 22 by Feldkamp from 1969 [54] for the pressure differential does not lead to any significant change in the gas crossover as it predicts negligible pressure differential between the half-cells at 7 bar. This indicates that pressure differential effects become more pronounced at high pressures, and a balanced pressure operation is important to reduce the gas crossover. The gas crossover due to differential pressure is not included in the model in Ref. [14]. In the dynamic switching operation, it is observed that a pressure

differential of 300 mbar (as an approximation) between the cathodic and anodic half-cells results in an excellent agreement between the experimental anodic hydrogen content (triangles) and the impurities obtained from the model (continuous cyan line). In addition, good agreement is observed between the experimental (circles) and simulated anodic hydrogen content (black dashed dotted line) for mixed electrolyte cycles for a period of 72 h. Considering the differential pressure between the half-cells leads to excellent agreement between the model (red dashed line) and experimental results. This shows that the model can be applied to more realistic cases with a fluctuating current driven by renewable energy sources, as opposed to perfectly monitored laboratory conditions. To demonstrate the sensitivity of the model to different fluctuating current density profiles, two other current densities were randomly generated using the
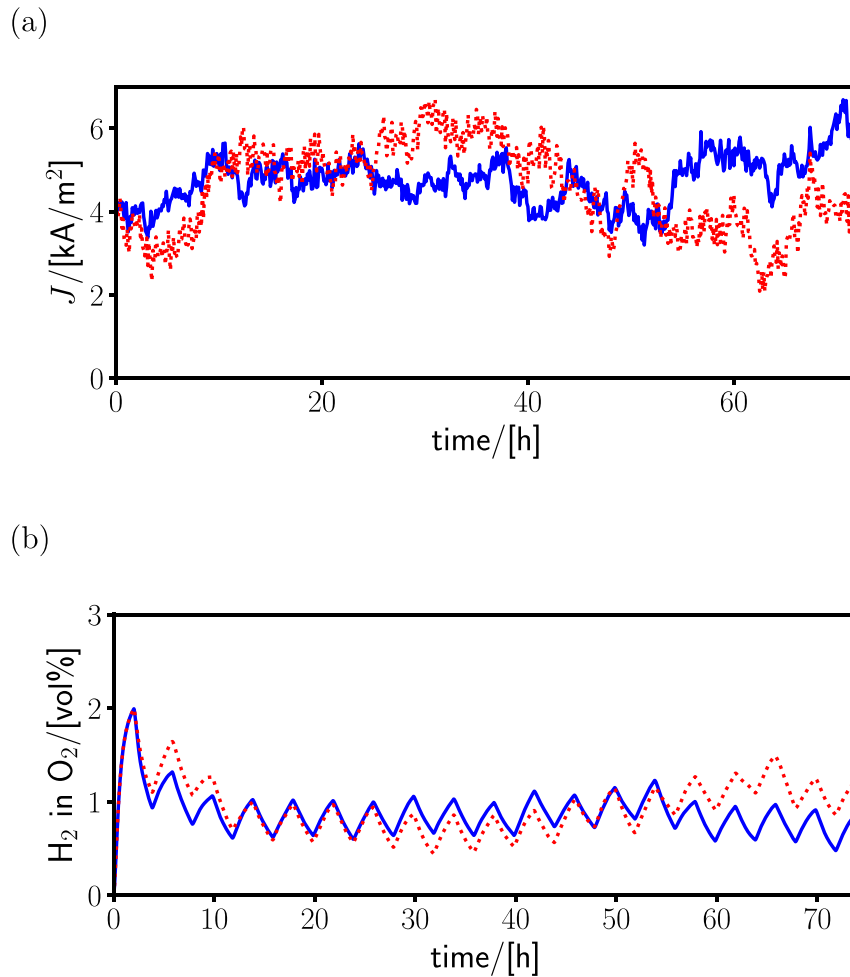
(a)

(b)

Fig. 8 − (a) Randomly-generated current density profiles for 72 h using the ARMA approach [57] as reported in Ref. [13]. The dynamic model was run using the synthetic current densities from subfigure (a). The dynamic model corresponds to the experimental setup by Brauns et al. [13] at P = 7 bar, and T = 60 °C. The corresponding impurities obtained from the simulations are shown in (b). The dashed and dotted lines (impurities) in subfigure (b) correspond to the dashed and dotted lines (current densities) in subfigure (a), respectively.

autoregressive-moving-average (ARMA) model from Refs. [13,57]. The randomly generated currents and the results are shown in Fig. 8. In this figure, the sensitivity of the model is shown with respect to fluctuating current from renewable sources. It is observed that the gas crossover model can respond to different current fluctuations which plays an important role in safe operation of the AWE.

Single cell model sensitivity analysis

A sensitivity analysis is performed to study the dynamic response of the system by changing operating conditions or the design characteristics of the cell. Eq. 14 is used to impose boundary conditions corresponding to mixed electrolyte flows. The operating conditions include the variation of the liquid volumetric flow rate, temperature, mass fraction of KOH, and the volume of the separator tanks. The models with the varying input parameters are compared to the base model in Section Mathematical Model. The input parameters of the base model are listed in Table 4.

In Fig. 9, the sensitivity analysis due to the variation of the operating conditions is presented. More specifically, the varying operating conditions include the liquid flow rate $\dot{V}_L$ (Fig. 9(a)), the temperature T of the process (Fig. 9(b)), the mass fraction of KOH (Fig. 9(c)), and the liquid $V_{liq}^{sep,j}$ and gaseous volume in the gas separator $V_{gas}^{sep,j}$ (Fig. 9(d)). The models with the varying operating conditions are compared with the base model in Table 4 (black dashed line). In Fig. 9(a), the anodic hydrogen content is shown for different electrolyte flow rates. It is observed that an increase in the liquid flow rate results in a higher anodic hydrogen content when the system reaches steady state. An increase in the liquid flow rate corresponds to higher electrolyte mixing leading to a higher convective mass transfer (Eq. (1) to 6). Therefore, the bulk concentration of hydrogen in the anodic half-cell increases as the liquid flow rate rises leading to a higher desorption flux (governed by higher supersaturation) into the gas phase. In a similar manner, reducing the liquid flow rate leads to a decrease in the anodic hydrogen content. Based on Fig. 9(a), it is observed

Table 4 – Input parameters of the base model for the sensitivity analysis.			
Variable	Symbol	Value	Units
KOH mass fraction	w_{KOH}	30	wt%
Liquid flow rate	$\dot{V}_L$	100	mL min^{-1}
Operating temperature	T	313.15	K
Operating pressure in the compartment j	p^j	101,325	Pa
Current density	J	1	kA m^{-2}
Anodic gas separator volume	V_{sep}^{ano}	1	L
Cathodic gas separator volume	V_{sep}^{cat}	1	L
Liquid volume in the anodic gas separator	$V_{liq}^{sep,ano}$	0.5	L
Liquid volume in the cathodic gas separator	$V_{liq}^{sep.cat}$	0.5	L
Hydrogen gas evolution efficiency	f_{G,H_2}	0.875	–
Oxygen gas evolution efficiency	f_{G,O_2}	0.830	–

(a)　　　　　　　　　　　　　　(b)

(c)　　　　　　　　　　　　　　(d)
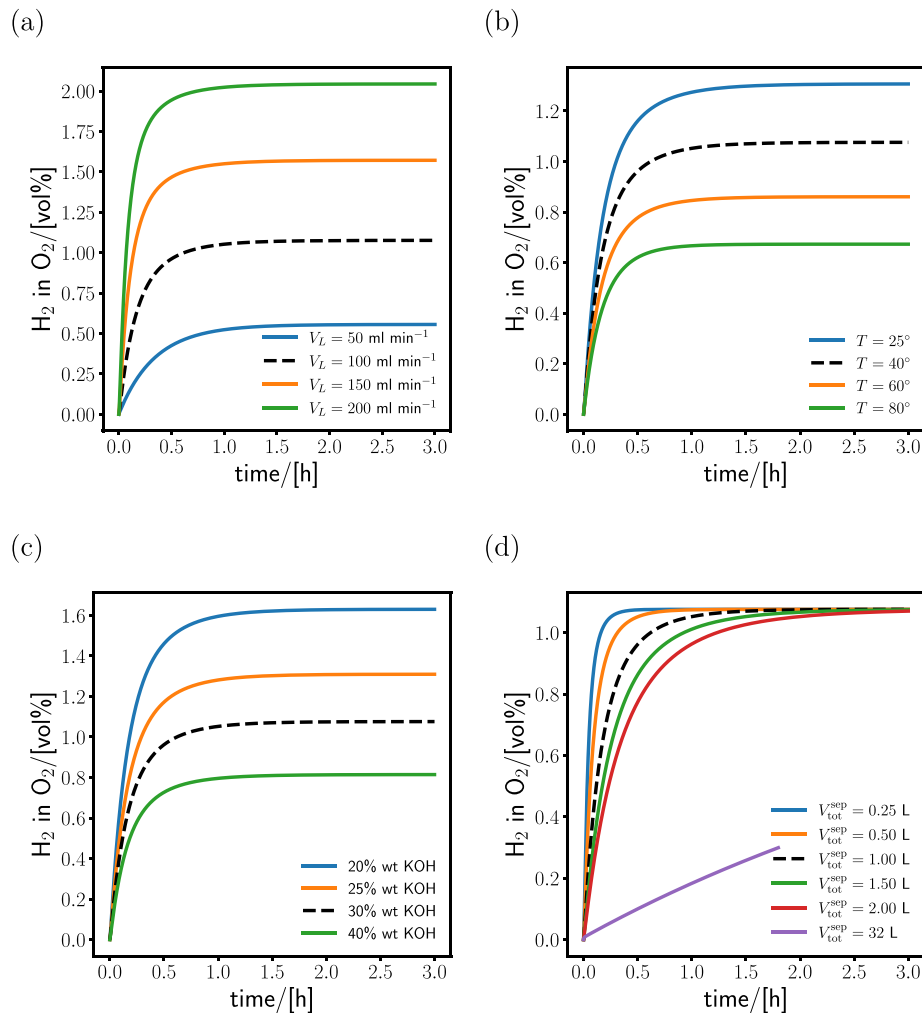
Fig. 9 – **Changes in the dynamic response of the system as a result of changing one of the operating conditions or design characteristics compared to Table 4: (a) Liquid flow rate. (b) Temperature. (c) KOH wt%. (d) Volume of the separator tank.**

that in the current range of flow rates, the transition time to steady state is not significantly affected. In Fig. 9(b), the change in the anodic hydrogen content is provided with respect to the variation of the cell temperature. It is observed that an increase in temperature leads to a decrease in the anodic hydrogen content. Based on the available gas solubility data in electrolyte solutions [58], one can conclude that the

solubility of hydrogen and oxygen in liquid electrolyte decreases with temperature which leads to a higher supersaturation in the electrolyte for a certain current density. A higher desorption flux of hydrogen to the gas phase in the cathodic half-cell (as a result of temperature increase) reduces the mole fraction of the crossover oxygen (impurity). Similarly, due to a higher desorption flux of oxygen into the gas phase in the

anodic half-cell, the mole fraction of the crossover hydrogen (impurity) reduces. Higher temperatures also lead to a higher hydrogen and oxygen diffusivity [49]. However, the results indicate that the effect of increased desorption flux at higher temperature is dominant compared to the increased hydrogen or oxygen diffusion flux through the membrane. This results in a lower gas crossover rate. When reducing the temperature, the opposite behavior is observed. The variation of the temperature does not affect the transition time to the steady state. When considering Fig. 9(b), it is important to distinguish between the concepts liquid phase solubilities, and impurities (mole fractions) in the gas phase. In Fig. 9(c), the effect of mass fraction of aqueous KOH solution on the anodic content is shown. It is shown that increasing the mass fraction of KOH leads to a decrease in the anodic hydrogen content. Due to the well-known salting out effect [45], the solubility of hydrogen and oxygen in the bulk electrolyte decreases. This causes a higher desorption flux of hydrogen in the cathodic half-cell and a higher desorption flux of oxygen in the anodic half-cell to the gas phase. Consequently, the mole fraction of hydrogen in anodic oxygen decreases with increasing KOH mass fraction. It is observed that in the current range of mass fractions, the transition time to the steady-state is not affected. In Fig. 9(d), the dynamic response of the anodic hydrogen content is shown in terms of the total geometrical volume of the separator tanks. The liquid volume of the electrolyte in the gas separator is 50% of the geometrical volume of the separator tank. It is noticed that an increase in the geometrical volume results in a longer transition time to the steady-state. An increase in the geometrical volume of the gas separator leads to an increase of both the liquid and gaseous volume inside the gas separator. Therefore, it causes a slower response in the dissolved species in the liquid electrolyte and a slower response in the outlet partial pressures of the species in the gas separator. This observation can be explained based on the ODEs of Eqs. 5 and 6. The transition time of the anodic hydrogen content presents a strong dependency on the

gaseous volumetric flow rate. Since the response time of the bulk concentration increases with increasing the volume of the separator tank, the gaseous volumetric flow rate will develop slower. Therefore, when the volume of the separator tank increases, the anodic hydrogen content reaches its steady-state value slower. On the contrary, when the volume of the gas separators decreases, the anodic hydrogen content will reach its steady-state value faster as a result of the bulk concentration and the partial pressures in the gas separator developing faster.

Evaluating switching time and startup modes for n_{cell} stacks

The anodic hydrogen content is computed for stacks with 5 and 20 cells, and the results are compared to those obtained from a single cell. To showcase the influence of the separator tank volumes, two separator tanks of 40 L are considered. For the cells, the same design characteristics in Table 2 are considered. The total flow of the stack is computed based on the flow of a single cell (330 ml min^{-1} per half-cell) times the number of cells. Simulations were performed for a switching time of 1 h (between mixed and separated electrolyte flows), and current density of $J = 0.2$ kAm^{-2}. The total simulation time is 20 h. The results are shown in Fig. 10. It can be seen that in Fig. 10(a), the anodic hydrogen content of the 20-cell stack is highest during the same startup time compared to a single cell and the 5-cell stack. Assuming a design threshold of 2% for the anodic hydrogen content (50% of explosion safety limit), it is concluded from Fig. 10(a) that a switching time less than an hour is necessary for the 20-cell stack. For the 5-cell stack, the simulation results show that both the simulation time and the anodic hydrogen content are favourable (below 2%). For a single cell system, the results show that the system anodic hydrogen content is building up very gradually. This indicates that the sizing of the separator tanks are not suited for the single cell system. This analysis shows that the dynamic response obtained from the transient model of the stack can
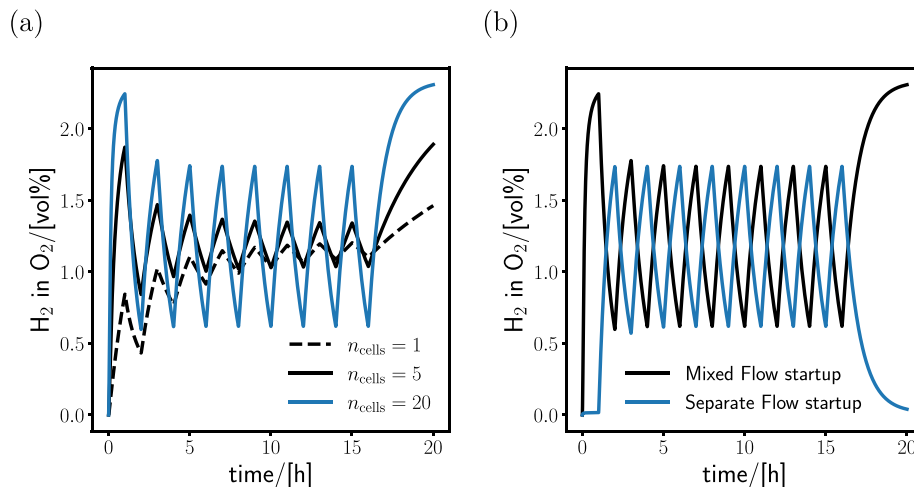
(a)

(b)

Fig. 10 − (a) Calculated anodic hydrogen contents with different stack sizes (1−20 cells) with a dynamic switching time of 1 h. The following average impurities are obtained in the anodic compartment: 1.02%vol for the single-cell stack, 1.19%vol for 5-cell stack, and 1.19%vol for 20-cell stack. (b) Comparing the anodic hydrogen content with separate and mixed flow startups for 20-cell stack. The anodic hydrogen content remains below 2% during separated startup with an average value of 1.17%vol. The current density used in this simulation is $J = 0.2$ kAm^{-2}. For all cases, a switching time of 1 h was used.

be directly used for sizing of the separator tanks and/or the stacks. In Fig. 10(b), the anodic hydrogen content is shown for the same stack of 20 cells, with two different startups, one with mixed electrolyte cycles, and one with separated electrolyte flows. It is clear from the results, that the a threshold of 2% is avoided when the system is started with separated flows with 1 h cycle time for switching between mixed and separated electrolyte cycles. The average anodic hydrogen content during this dynamic switching remains the same. The results in Fig. 10 are an example of how the transient model can be used both for sizing of the separator tanks and safe operation of the system with regards to explosion regulations.

Conclusions

To predict gas crossover in alkaline electrolysis, we have developed a transient model as an extension of the steady-state model developed by Haug et al. [14,15]. One can perform simulations for a specific case of a single-cell electrolysis stack or a multi-cell stack. Due to the dynamic nature of the model, gas crossover can be predicted for mixed anolyte and catholyte flows, separated flows, or a combination thereof in time. The model is validated for the single-cell case using the data from the experimental setup and operating conditions provided by Haug et al. The average anodic content obtained from the dynamic mixing/separating of electrolyte flows ($y_{H_2}^{avg,mod} = 0.29$ vol%) is in good agreement with the experimental results reported by Haug et al. ($y_{H_2}^{avg} = 0.31$ vol%) [14]. Due to the CSTR assumption, the model does not capture local supersaturation near the electrode surface leading to an underestimation of the anodic hydrogen content. The model is also validated with the experimental results by Brauns et al. [13] at 7 bar. Brauns et al. have used a fluctuating current density profile representing wind as an input for the electrolyzer, and have measured the anodic hydrogen content for separated and mixed electrolyte cycles. Good agreement is observed between the results obtained from the model and the reported experimental data for a period of 72 h. It is important to note that excellent agreement with the experimental results is obtained when considering the contribution of the pressure differential between the half-cells to the overall gas crossover. The dynamic response of the model to the gas crossover is studied by changing the electrolyte flow rates, temperature, mass fraction of the electrolyte and the total volume of the separator tanks. The results obtained from the simulations indicate a strong dependency of the transition time to steady-state conditions on the size of the separator tanks. The volume of the half-cells can influence the transition time to steady-state conditions. In this model, the gas evolution efficiency acts as a lumped parameter capturing both the effect of the crossover through the separator and electrolyte mixing. The extended multi-cell model is used to compute the gas crossover as a function of different stack sizes from 1 to 20 cells. It is observed that at the startup, the rate of building up impurities is highest for the 20-cell stack. This rate can be reduced or modified by using a smaller switching time or starting up the electrolyzer using the separated electrolyte cycles. Depending on the requirements for the impurities, the model can be used

as a tool to adjust the operation of the mixed/separated electrolyte cycles for different stack and separator tank sizes. Furthermore, the model predicts different anodic hydrogen contents depending on whether the system starts up with mixed or separated electrolyte cycles.

Declaration of competing interest

Nomenclature

Constants

F	Faraday's constant	96,485 (C mol^{-1})
g	Gravitational *acceleration*	9.81 (m/s^2)
M_{H_2O}	Molar mass of water	18.01 (g mol^{-1})
M_{KOH}	Molar mass of KOH	56.10 (g mol^{-1})
n	Charge *transfer*	(−)
R	Universal gas constant	8.314 (J mol^{-1} K^{-1})

Greek symbols

δ_L	Liquid film thickness (m)
γ	Surface tension of KOH concentrated liquid electrolyte (N m^{-1})
μ_L	Dynamic *viscosity* of KOH liquid electrolyte (Pa s)
ν_i	Stoichiometric coefficient of species i
ρ_{H_2O}	Water density (kg m^{-3})
ρ_L	Density of KOH liquid electrolyte (kg m^{-3})
τ	Tortuosity of the separator
θ	Electrolyte temperature (°C)
ϵ	Porosity of the separator
$\epsilon_{g,out}^j$	Gas hold-up fraction at the outlet of compartment j
ϵ_g^j	Gas hold-up fraction inside the compartment j

Symbols

$\dot{n}_{R,i}^j$	Reaction rate of species i in compartment j (mol s^{-1})
$\dot{V}_{mix}$	Liquid flow rate under mixed-mode operation (m^3 s^{-1})
$\dot{V}_G^j$	Outlet gaseous volumetric flow rate in compartment j (m^3 s^{-1})
$\dot{V}_L^j$	Inlet liquid volumetric flow rate in compartment j (m^3 s^{-1})
A_d	Separator area (m^2)
Ael	Electrode area (m^2)
A_{GL}^j	Gas liquid interface in compartment j (m^2)
$c_{in,i}^j$	Inlet concentration of product i in compartment j (mol m^{-3})
$c_{out,i}^{sep,j}$	Outlet concentration of species i in the gas separator of the compartment j (mol m^{-3})
$c_{out,i}^j$	Outlet concentration of product i in compartment j (mol m^{-3})
$c_{i,H_2O}^{*,j}$	Equilibrium concentration of species i in pure water in compartment j (mol m^{-3})
$c_i^{*,j}$	Equilibrium concentration of species i in compartment j (mol m^{-3})

c_i^{mix}	Inlet mixed-mode concentration of species i (mol m^{-3})
d_d	Thickness of the separator (m)
d_b^j	Diameter of bubble in compartment j (m)
$Di_{,\theta}$	Molecular diffusivity of species i, at temperature θ in the KOH liquid electrolyte (m^2 s^{-1})
D_i^{eff}	Effective diffusivity of species i (m^2 s^{-1})
$f_{G,i}$	Gas evolution efficiency of species i (–)
$h_{liq}^{sep,j}$	Liquid volume fraction in the gas separator of the compartment j (%)
H_i	Henry's coefficient of species i (atm)
i	Species, H_2 or O_2
J	Applied current density (A m^{-2})
j	Corresponding anodic or cathodic compartment/ separatortank
$k_{L,i}^j$	Mass transfer coefficient of the gas-liquid film of species i in compartment j(m s^{-1})
$K_{S,i}$	Sechenov constant of species i
m	Molality of KOH (mol kg^{-1})
$N_{cross,i}$	Crossover flux of species i through the separator (mol m^{-2} s^{-1})
$N_{phys,i}^j$	Physisorption mass flux of species i in compartment j (mol m^{-2} s^{-1})
$N_{i,gas}^{j,sep}$	Moles of species i in the gaseous volume of gas separator of the compartment j (mol)
$N_{i,gas}^j$	Moles of species i in the gaseous volume of compartment j (mol)
$N_{i,liq}^{j,sep}$	Moles of species i in the liquid volume of gas separator of the compartment j (mol)
$N_{i,liq}^j$	Moles of species i in the liquid volume of compartment j (mol)
p_{H_2O}	Water vapour partial pressure (Pa)
p^j	Pressure exerted on the liquid electrolyte by means of a pump in compartment j (Pa)
$p_{in,i}^j$	Inlet partial pressure of species i in the compartment j (Pa)
$p_{out,i}^{sep,j}$	Outlet partial pressure of species i in the gas separator of the compartment j (Pa)
$p_{out,i}^j$	Outlet partial pressure of species i in the compartment j (Pa)
p_{tot}^j	Total pressure in the compartment j (Pa)
S_b^j	Surface area of a single bubble in compartment j(m^2)
T	Temperature (K)
t_{switch}	Switching time (min)
t_{tot}	Total time of the experiment (h)
V_b	Volume of a single bubble in compartment j (m^3)
V_{hcell}	Geometrical volume of the half cell (m^3)
$V_{gas}^{sep,j}$	Gaseous volume inside the gas separator of its associated compartment j (m^3)
$V_{gas}^{tot,j}$	Gaseous volume of the half-cell and the gas separator of compartment j (L)
V_{gas}^j	Gaseous volume inside the compartment j (m^3)
$V_{liq}^{sep,j}$	Liquid volume inside the gas separator of its associated compartment j (m^3)
$V_{liq}^{tot,j}$	Liquid volume of the half-cell and the gas separator of compartment j (L)
V_{liq}^j	Liquid volume inside the compartment j (m^3)
V_{sep}^j	Geometrical volume of the gas separator of its associated compartment j (m^3)

w_{KOH}	Mass fraction of potassium hydroxide in the electrolyte solution
$y_{H_2}^{avg,mod}$	Average calculated anodic hydrogen content (vol%)
$y_{H_2}^{avg}$	Average experimental anodic hydrogen content (vol %)
y_i	volume fraction of species i (vol%)

REFERENCES

[1] World energy outlook. Tech. rep. International Energy Agency; 2021. https://www.oecd-ilibrary.org/content/publication/14fcb638-en. accessed on 15-12-2022.

[2] Wappler M, Unguder D, Lu X, Ohlmeyer H, Teschke H, Lueke W. Building the green hydrogen market—current state and outlook on green hydrogen demand and electrolyzer manufacturing. Int J Hydrogen Energy 2022;47:33551–70.

[3] Fawzy S, Osman AI, Doran J, Rooney DW. Strategies for mitigation of climate change: a review. Environ Chem Lett 2020;18:2069–94.

[4] Global hydrogen review 2022. Tech. rep. International Energy Agency; 2022. https://www.iea.org/reports/global-hydrogen-review-2022. accessed on 15-12-2022

[5] Ishaq H, Dincer I, Crawford C. A review on hydrogen production and utilization: challenges and opportunities. Int J Hydrogen Energy 2022;47:26238–64.

[6] Arsad A, Hannan M, Al-Shetwi AQ, Hossain M, Begum R, Ker PJ, Salehi F, Muttaqi K. Hydrogen electrolyser for sustainable energy production: a bibliometric analysis and future directions. Int J Hydrogen Energy 2023;48:4960–83.

[7] Chatenet M, Pollet BG, Dekel DR, Dionigi F, Deseure J, Millet P, Braatz RD, Bazant MZ, Eikerling M, Staffell I, et al. Water electrolysis: from textbook knowledge to the latest scientific strategies and industrial developments. Chem Soc Rev 2022;51:4583–762.

[8] Trasatti S. Water electrolysis: who first? J Electroanal Chem 1999;476:90–1.

[9] Karacan C, Lohmann-Richters FP, Keeley GP, Scheepers F, Shviro M, Müller M, Carmo M, Stolten D. Challenges and important considerations when benchmarking single-cell alkaline electrolyzers. Int J Hydrogen Energy 2022;47:4294–303.

[10] Tjarks G, Mergel J, Stolten D. Dynamic operation of electrolyzers – systems design and operating strategies. John Wiley & Sons, Ltd; 2016. p. 309–30. Ch. 14.

[11] Kojima H, Nagasawa K, Todoroki N, Ito Y, Matsui T, Nakajima R. Influence of renewable energy power fluctuations on water electrolysis for green hydrogen production. Int J Hydrogen Energy 2023;48:4572–93.

[12] Lange H, Klose A, Lippmann W, Urbas L. Technical evaluation of the flexibility of water electrolysis systems to increase energy flexibility: a review. Int. J. Hydrogen Energy 2023;48:15771–83.

[13] Brauns J, Turek T. Experimental evaluation of dynamic operating concepts for alkaline water electrolyzers powered by renewable energy. Electrochim Acta 2022;404:139715.

[14] Haug P, Kreitz B, Koj M, Turek T. Process modelling of an alkaline water electrolyzer. Int J Hydrogen Energy 2017;42:15689–707.

[15] Haug P, Koj M, Turek T. Influence of process conditions on gas purity in alkaline water electrolysis. Int J Hydrogen Energy 2017;42(15):9406–18.

[16] Brauns J, Turek T. Alkaline water electrolysis powered by renewable energy: a review. Processes 2020;8.

[17] Ren Z, Wang J, Yu Z, Zhang C, Gao S, Wang P. Experimental studies and modeling of a 250-kw alkaline water electrolyzer for hydrogen production. J Power Sources 2022;544:231886.

[18] Hydrogen generators using water electrolysis — industrial, commercial, and residential applications, International standard. Geneva, CH: International Organization for Standardization; 2019. https://www.iso.org/standard/69212.html. access date 15-12-2022.

[19] de Groot MT, Kraakman J, Garcia Barros RL. Optimal operating parameters for advanced alkaline water electrolysis. Int J Hydrogen Energy 2022;47:34773–83.

[20] Trinke P, Haug P, Brauns J, Bensmann B, Hanke-Rauschenbach R, Turek T. Hydrogen crossover in PEM and alkaline water electrolysis: mechanisms, direct comparison and mitigation strategies. J Electrochem Soc 2018;165:F502–13.

[21] Ligen Y, Vrubel H, Girault H. Energy efficient hydrogen drying and purification for fuel cell vehicles. Int J Hydrogen Energy 2020;45:10639–47.

[22] Haug P. Experimental and theoretical investigation of gas purity in alkaline water electrolysis. Ph.D. thesis. In: Dissertation, clausthal-zellerfeld. 2019. Technische Universität Clausthal; 2019.

[23] Lee J, Alam A, Ju H. Multidimensional and transient modeling of an alkaline water electrolysis cell. Int J Hydrogen Energy 2021;46:13678–90.

[24] Aboukalam da Cruz MH, Etancelin M, Marias F, Reneaume J-M, Sochard-Reneaume S, Serra S. Dynamic modelling of an alkaline water electrolysis system and optimization of its operating parameters for hydrogen production. Int J Hydrogen Energy 2023;48:12982–99.

[25] Sakas G, Ibáñez-Rioja A, Ruuskanen V, Kosonen A, Ahola J, Bergmann O. Dynamic energy and mass balance model for an industrial alkaline water electrolyzer plant process. Int J Hydrogen Energy 2022;47:4328–45.

[26] David M, Alvarez H, Ocampo-Martinez C, Sánchez-Peña R. Dynamic modelling of alkaline self-pressurized electrolyzers: a phenomenological-based semiphysical approach. Int J Hydrogen Energy 2020;45:22394–407.

[27] Hammoudi M, Henao C, Agbossou K, Dubé Y, Doumbia M. New multi-physics approach for modelling and design of alkaline electrolyzers. Int J Hydrogen Energy 2012;37:13895–913.

[28] Documentation S. Simulation and model-based design. 2020. https://www.mathworks.com/products/simulink.html.

[29] Sánchez M, Amores E, Rodríguez L, Clemente-Jul C. Semi-empirical model and experimental validation for the performance evaluation of a 15 kW alkaline water electrolyzer. Int J Hydrogen Energy 2018;43:20332–45.

[30] Optimization toolbox user's guide. The MathWorks, USA: MathWorks, Inc.; 2016.

[31] Smith R. Chemical process: design and integration. Wiley; 2005. https://books.google.nl/books?id=cdyiWR0d1o8C.

[32] Wang J. Analytical electrochemistry. 3rd ed. New Jersey, USA: John Wiley & Sons, Ltd; 2006.

[33] Vogt H. Gas-evolving electrodes. In: Comprehensive treatise of electrochemistry. Boston, MA: Springer US; 1983. p. 445–89. https://doi.org/10.1007/978-1-4615-6690-8_7.

[34] Vogt H. Studies on gas-evolving electrodes: the concentration of dissolved gas in electrolyte bulk. Electrochim Acta 1985;30:265–70.

[35] Vogt H. Mechanisms of mass transfer of dissolved gas from a gas-evolving electrode and their effect on mass transfer coefficient and concentration overpotential. J Appl Electrochem 1989;19:713–9.

[36] Vogt H, Kreysa G, Vasudevan S, Wüthrich R, Abou Ziki JD, El-Haddad R. Electrochemical reactors. In: Ullmann's encyclopedia of industrial chemistry. Weinheim, Germany: Wiley-VCH Verlag GmbH & Co. KGaA; 2014. p. 1–49.

[37] Vogt H. The rate of gas evolution at electrodes—II. An estimate of the efficiency of gas evolution on the basis of bubble growth data. Electrochim Acta 1984;29:175–80.

[38] Rahbari A, Brenkman J, Hens R, Ramdin M, van den Broeke LJP, Schoon R, Henkes R, Moultos OA, Vlugt TJH. Solubility of water in hydrogen at high pressures: a molecular simulation study. J Chem Eng Data 2019;64:4103–15.

[39] Rahbari A, Garcia-Navarro JC, Ramdin M, van den Broeke LJP, Moultos OA, Dubbeldam D, Vlugt TJH. Effect of water content on thermodynamic properties of compressed hydrogen. J Chem Eng Data 2021;66:2071–87.

[40] Luis P. Fundamental modeling of membrane systems: membrane and process performance. 1st ed. Amsterdam, The Netherlands: Elsevier; 2018.

[41] de Haan AB, Eral HB, Schuur B. Industrial separation processes fundamentals. Berlin, Boston: De Gruyter; 2020.

[42] Bird RB, Stewart WE, Lightfoot EN. Transport phenomena. 2nd ed. New York, USA: John Wiley & Sons, Inc.; 2007.

[43] Himmelblau DM. Solubilities of inert gases in water. $0°$ C. To near the critical point of water. J Chem Eng Data 1960;5:10–5.

[44] Rischbieter E, Schumpe A, Wunder V. Gas solubilities in aqueous solutions of organic substances. J Chem Eng Data 1996;41:809–12.

[45] Schumpe A. The estimation of gas solubilities in salt solutions. Chem Eng Sci 1993;48:153–8.

[46] Kell GS. Density, thermal expansivity, and compressibility of liquid water from $0°C$ to $150°C$ Correlations and tables for atmospheric pressure and saturation reviewed and expressed on 1968 temperature scale. J Chem Eng Data 1975;20:97–105.

[47] Liu X, Schnell SK, Simon J-M, Krüger P, Bedeaux D, Kjelstrup S, Bardow A, Vlugt TJH. Diffusion coefficients from molecular dynamics simulations in binary and ternary mixtures. Int J Thermophys 2013;34:1169–96.

[48] Celebi AT, Jamali SH, Bardow A, Vlugt TJH, Moultos OA. Finite-size effects of diffusion coefficients computed from molecular dynamics: a review of what we have learned so far. Mol Simulat 2021;47:831–45.

[49] Tham MJ, Walker RD, Gubbins KE. Diffusion of oxygen and hydrogen in aqueous potassium hydroxide solutions. J Phys Chem 1970;74:1747–51.

[50] Habibi P, Rahbari A, Blazquez S, Vega C, Dey P, Vlugt TJH, Moultos OA. A new force field for OH– for computing thermodynamic and transport properties of H2 and O2 in aqueous NaOH and KOH solutions. J Phys Chem B 2022;126:9376–87.

[51] LeRoy RL, Bowen CT, LeRoy DJ. The thermodynamics of aqueous water electrolysis. J Electrochem Soc 1980;127:1954–62.

[52] Balej J. Water vapour partial pressures and water activities in potassium and sodium hydroxide solutions over wide concentration and temperature ranges. Int J Hydrogen Energy 1985;10:233–43.

[53] Guggenheim EA. Interfacial tension of curved interface. In: Thermodynamics: an advanced treatment for chemists and physicists. 7th ed. Amsterdam, North-Holland: Elsevier; 1985. p. 50–3. Ch. 1.

[54] Feldkamp K. Die Oberflächenspannung wäßriger NaOH- und KOH-Lösungen. Chem Ing Tech 1969;41(21):1181–3. https://doi.org/10.1002/cite.330412107.

[55] Gilliam R, Graydon J, Kirk D, Thorpe S. A review of specific conductivities of potassium hydroxide solutions for various concentrations and temperatures. Int J Hydrogen Energy 2007;32:359–64.

[56] SciPy Integration and Odes. scipy.integrate.odeint, https://docs.scipy.org/doc/scipy/reference/generated/scipy.integrate.odeint.html#scipy-integrate-odeint; 2022. accessed on 15-12-2022.

[57] Chen J, Rabiti C. Synthetic wind speed scenarios generation for probabilistic analysis of hybrid energy systems. Energy 2017;120:507–17.

[58] J. Walker, R. D., A study of gas solubilities and transport properties in fuel cell electrolytes, Tech. rep., Florida Univ. Gainesville, FL, United States (2 1968) URL https://ntrs.nasa.gov/citations/19690031817.

[59] Krause B, Vogt H. Effect of operational parameters on gas evolution in electrolyte bulk: possibilities for lowering interelectrode resistance. J Appl Electrochem 1985;15(4):509—15.